Research Square

Preprints are preliminary reports that have not undergone peer review.
They should not be considered conclusive, used to inform clinical practice,
or referenced by the media as validated information.

Satellite-observed contrail coverage over Europe and the North Atlantic in 2023

Irene Ortiz

irortiza@ing.uc3m.es

Universidad Carlos III de Madrid https://orcid.org/0009-0007-2023-5930

Ermioni Dimitropoulou

Royal Meteorological Institute of Belgium

Pierre de Buyl

Royal Meteorological Institute of Belgium

Nicolas Clerbaux

Royal Meteorological Institute of Belgium

Hugues Brenot

Royal Belgian Institute for Space Aeronomy

Jeroen van Gent

Royal Belgian Institute for Space Aeronomy

Javier García-Heras

Carlos III University of Madrid

Manuel Soler

Carlos III University of Madrid

Research Article

Keywords: Contrail coverage, radiative forcing, satellite observations, aviation impacts

Posted Date: November 10th, 2026

DOI: https://doi.org/10.21203/rs.3.rs-9370812/v2

License: This work is licensed under a Creative Commons Attribution 4.0 International License.
Read Full License

Additional Declarations: The authors declare no competing interests.

Satellite-observed contrail coverage over Europe and the North Atlantic in 2023

Irene Ortiz[1], Ermioni Dimitropoulou[2], Pierre de Buyl[1], Nicolas Clerbaux[2], Javier García-Heras[2], Jeroen van Gent[3], Hugues Brenot[3], and Manuel Soler[1]

[1]Universidad Carlos III de Madrid
[2]Royal Meteorological Institute of Belgium
[3]Royal Belgian Institute for Space Aeronomy

Correspondence: Irene Ortiz (irortiza@ing.uc3m.es)

Abstract. Geostationary satellite observations enable continuous monitoring of contrail coverage and its associated radiative effects, capturing their diurnal and seasonal variability over extensive spatial domains. In this work, we investigate linear contrails over the Euro–Atlantic region using Meteosat Second Generation (MSG) observations throughout 2023. Contrails are detected using a neural network trained on manually labeled satellite imagery, cloud properties are derived from MSG retrievals calibrated through an empirical linear regression model, and radiative forcing is estimated using radiative-transfer lookup tables. The results reveal contrasting regional diurnal patterns in contrail coverage, with two daily maxima over the North Atlantic and a dominant morning peak over continental Europe. Seasonally, coverage peaks in spring and decreases by 37% in summer, despite 16% higher cruise traffic. To quantify the associated radiative forcing, the proposed retrieval method estimates mean contrail cloud-top height, optical depth, and effective ice-crystal radius of 11.57 km, 0.309, and 28.8 μm, respectively. The annual mean net forcing across contrail pixels is -1.4 $\mathrm{W\,m^{-2}}$ during daytime and $+32.7$ $\mathrm{W\,m^{-2}}$ at night, resulting in a coverage-weighted annual mean of $+2.85$ $[1.09–6.21]$ $\mathrm{mW\,m^{-2}}$ over the study region. Atlantic waters account for approximately 78% of this warming, suggesting a disproportionate contribution from transatlantic traffic. Overall, the findings reveal substantial regional differences in satellite-observed contrail coverage and radiative forcing, motivating further investigation into the influence of atmospheric conditions and air traffic in the reported trends.

1 Introduction

The aviation sector accounts for approximately 3.5%–4% of total global anthropogenic climate forcing (Lee et al., 2021; Klöwer et al., 2021), with approximately two-thirds estimated to arise from non-CO_2 effects (Lee et al., 2021). Contrails and the contrail-cirrus clouds that develop from them are recognized as the largest individual non-CO_2 contribution, and also one of the most uncertain (Lee et al., 2021). Contrails form in the cold upper troposphere when moist aircraft exhaust mixes with ambient air, causing droplets to condense and rapidly freeze into ice crystals (Kärcher et al., 2015). In ice-supersaturated air they can persist and spread into extensive contrail-cirrus fields (Schumann and Heymsfield, 2017; Minnis et al., 1998). Like natural cirrus, they perturb the Earth's radiation budget in two competing ways: they reflect incoming shortwave radiation, which cools, and they trap outgoing longwave radiation, which warms. Their net effect depends on the balance between the

two (Kärcher, 2018).

This balance is controlled by several factors that vary strongly in space and time. Forcing generally increases with optical depth and coverage (Meerkötter et al., 1999). Smaller ice particles and habits that scatter more sideways enhance daytime shortwave cooling (Schumann et al., 2012), whereas higher, colder contrails produce stronger longwave warming (Wang et al., 2024; Wolf et al., 2023). Overlap with other clouds weakens both components but reduces the shortwave more, which can increase net warming (Sanz-Morère et al., 2021). Lifetime matters most of all: where persistence is limited by the surrounding atmosphere, the cumulative energy forcing scales approximately quadratically with it (Schumann and Heymsfield, 2017). Because these controls differ across regions, seasons, and times of day, and because shortwave cooling acts only in daylight, quantifying contrail climate effects requires resolving how contrail coverage and forcing vary through the diurnal and seasonal cycles. Current global studies rely largely on models and remain widely uncertain. Lee et al. (2021) estimated a contrail-cirrus radiative forcing of $111\ \mathrm{mWm^{-2}}$ in 2018 (5th–95th percentile range: 33–$189\ \mathrm{mWm^{-2}}$), whereas Teoh et al. (2024) obtained $62.1\ \mathrm{mWm^{-2}}$ for 2019 (34.8–$74.8\ \mathrm{mWm^{-2}}$) using the Contrail Cirrus Prediction model (CoCiP) (Schumann, 2012). As modelling approaches increasingly constrain these values (Bickel et al., 2025), observational evaluation is needed to test their robustness and trends.

Multispectral satellite observations enable the distinction between linear contrails and natural cirrus in infrared imagery (Mannstein et al., 1999), while providing the extensive spatial coverage required for large-scale assessments. Low-Earth-orbit (LEO) satellites provide the high spatial resolution required to detect relatively thin linear contrails and have enabled regional to hemispheric assessments of contrail coverage and radiative forcing, with Northern Hemisphere mean forcing estimates of different years ranging between $8 - 10.6\ \mathrm{mWm^{-2}}$ (Spangenberg et al., 2013; Duda et al., 2019). They have also revealed strong diurnal contrasts, including about 80% higher early-morning than afternoon linear contrail coverage over the United States (Palikonda et al., 2005) and nighttime forcing 3.6 times greater than daytime forcing (Spangenberg et al., 2013). However, the limited number of daily overpasses provides only sparse sampling of the diurnal cycle, potentially overlooking important variations and highlighting the need for higher-temporal-resolution observations to fully characterize these patterns.

Geostationary satellites overcome this limitation by repeatedly observing the same region throughout the day. Although their coarser spatial resolution limits the detection of small or optically thin contrails (Euchenhofer et al., 2025; Mannstein et al., 2010), their high temporal resolution makes them particularly suitable for studying diurnal and seasonal variability. Early studies used geostationary observations to track individual contrail outbreaks over the United States and investigate their optical properties and radiative effects (Duda et al., 2001, 2004). More recently, automated detection methods have enabled the analysis of multi-year satellite records, particularly over the United States, to quantify variations in contrail coverage, including those associated with reduced air traffic during the COVID-19 pandemic (Meijer et al., 2022; Ng et al., 2024). Other recent studies have focused on analyzing the limitations of contrail detectability in geostationary imagery (Euchenhofer et al., 2025; Driver et al., 2025) and developing methods to extend the detectable lifetime of contrails (Sonabend-W et al., 2025). Despite these

advances, large-scale observational assessments jointly quantifying contrail coverage and radiative forcing across diurnal and seasonal cycles remain scarce, particularly over Europe and the North Atlantic. Two earlier studies provided valuable insights into these regions. Vazquez-Navarro et al. (2010) developed an automated contrail-tracking algorithm that was subsequently applied to one year of observations over Europe and the North Atlantic to estimate contrail lifetimes and radiative properties (Vázquez-Navarro et al., 2015). However, because contrails were initially identified in LEO imagery before being tracked in geostationary observations, the approach did not sample the entire contrail population observable from geostationary satellites or its complete diurnal cycle. Moreover, differences between the spatial distribution of tracked contrails and actual contrail coverage prevented the combination of shortwave and longwave forcing into a net radiative effect. Over the North Atlantic, Graf et al. (2012) used eight years of observations (2004–2011) to investigate aviation-related variations in contrail-cirrus coverage by comparing regions with high and low air traffic. Their analysis, however, directly estimated only the longwave effect, relying on model-derived shortwave-to-longwave ratios to infer the net radiative effect. More recent studies have focused either on large-scale contrail-coverage patterns (Dekoutsidis et al., 2023) or on the radiative properties of individual contrail outbreaks (Wang et al., 2023, 2024), rather than jointly characterizing their spatial and temporal variability. Thus, a long-term observational assessment integrating contrail coverage and net radiative forcing across both Europe and the North Atlantic, while addressing some methodological limitations above mentioned, remains lacking.

In this work, we provide such analysis using observations from the Spinning Enhanced Visible and InfraRed Imager (SEVIRI) aboard the Meteosat Second Generation (MSG) geostationary satellites (Section 2.1). Contrails are identified using a neural network trained on the large, manually annotated GOES-16 OpenContrails dataset (Ng et al., 2023a) and validated in Ortiz et al. (2025). We adapt this model to MSG/SEVIRI through transfer learning using a recently published, smaller dataset of manually labeled contrails over the study region (Santos Gabriel et al., 2026). Independent validation against this dataset demonstrates that the adapted model achieves performance comparable to that obtained with the original GOES-16 imagery (Section 3.1). The auxiliary cloud-property retrievals accompanying the manually labeled SEVIRI dataset, which are better suited to characterizing high-altitude ice clouds than the standard Optimal Cloud Analysis (OCA) products, enable us to develop a linear regression model to refine the SEVIRI OCA cloud properties on the yearly study (Section 3.2.1). The radiative forcing of detected contrails is estimated using the retrieved cloud properties and auxiliary atmospheric data through the lookup tables (Section 3.3) developed by Dimitropoulou et al. (2026), enabling efficient quantification of both shortwave and longwave radiative effects.

2 Data

The study uses the satellite imagery described in Section 2.1 to characterize contrail coverage, retrieve their physical properties, and estimate their radiative impact. The resulting spatial and temporal patterns are further compared with the flight data described in Section 2.2. An independent contrail benchmark dataset introduced in Section 2.3 was selected for the evaluation of the methods used in this work as well as for the calibration of the cloud retrievals.

2.1 Dataset for the 2023 contrail analysis

The satellite scenes used for studying contrails were acquired by SEVIRI onboard the MSG-3 and MSG-4 geostationary satellites of MSG series. Across its 12 spectral channels, SEVIRI provides radiances, reflectances, and equivalent blackbody brightness temperatures (BT) (Schmetz et al., 2002). Contrails can be identified in SEVIRI imagery using the false-color Ash RGB composite, which combines information from the 8.7, 10.8, and 12.0 μm thermal infrared channels. The red component, $BT_{12.0} - BT_{10.8}$, is particularly sensitive to differences in ice-crystal size and is commonly used to enhance young contrails relative to natural cirrus (Mannstein et al., 1999). The green component, $BT_{10.8} - BT_{8.7}$, provides additional sensitivity to thin ice clouds, while the blue component, $BT_{10.8}$, provides information related to cloud-top temperature (EUMETSAT, 2023). Together, these three channels make thin ice clouds, and specially contrails, visually distinguishable from the surrounding background.

SEVIRI has a nominal spatial resolution of 3 km at nadir for its 11 standard channels and 1 km for the High Resolution Visible (HRV) channel, which is not used in this study. Although it provides full-disk coverage, the present analysis is restricted to the Euro–Atlantic region (spanning latitudes 20–60°N and longitudes 60°W–40°E), which includes some of the most heavily trafficked airspace and is therefore particularly relevant for the purpose of studying contrails. Latitudes above 60°N, despite still covering parts of the North Atlantic and Europe, were excluded because viewing angles approaching or exceeding 80° introduce substantial geometric distortion, reducing contrail observability and detector performance (Section 3.1). In total, approximately 35,000 scenes were analyzed for 2023, corresponding to 96 observations per day at 15-min temporal resolution. All scenes were reprojected onto a common regular latitude–longitude grid at 0.04° resolution for the analysis.

2.2 Aircraft trajectory data

Flight data used to compare detected contrail coverage trends with aircraft crossings and schedules were obtained from the OpenSky Network (OpenSky, 2026) , which primarily relies on Automatic Dependent Surveillance–Broadcast (ADS-B) data transmitted by aircraft to ground-based receivers. Because $\sim 60\%$ of the domain is oceanic, where ADS-B coverage is sparse, missing trajectory segments were reconstructed using great-circle interpolation similar to Teoh et al. (2022).

2.3 Independent benchmark satellite dataset

The manually annotated dataset of Santos Gabriel et al. (2026) was used as the reference dataset because, to the best of our knowledge, it is the only publicly available SEVIRI dataset containing manual contrail labels. It comprises 140 MSG/SEVIRI scenes acquired between 10 February 2013 and 6 March 2024, mainly during the Meteosat-10 operational period, including 91 scenes with contrails, 995 annotated contrail segments, and 40,812 contrail pixels. Most annotated contrails extend over fewer than 60 pixels, with approximately half of the annotated pixels corresponding to daytime conditions. The scenes are distributed across the SEVIRI disk, covering different surface types and viewing geometries, with 77.6% of contrail pixels occurring over

ocean and 22.4% over land. Each scene was independently annotated by three labelers, and the dataset additionally provides ancillary cloud properties retrieved using the Cirrus Properties from SEVIRI (CiPS) algorithm. (Strandgren et al., 2017b)

3 Methods

The methodology consisted of three sequential steps: contrail pixel identification, cloud-property retrieval for the detected pixels, and radiative characterization using the retrieved properties.

3.1 Contrail Detection

Contrails are detected using the Co-scale Conv-Attentional Transformer (CoaT) segmentation architecture (Ortiz et al., 2025). The model was initialized with OpenContrails weights (Ng et al., 2023b) and fine-tuned on manually labeled SEVIRI Ash RGB scenes (Santos Gabriel et al., 2026) using transfer-learning (more details provided in supplementary Section 1). Of 140 available scenes, 83 were used for training, 34 for validation, and 23 for testing, with the test set consisting on 14 distinct UTC days and 7,832 labeled contrail pixels (definitions of all performance metrics are provided by Ortiz et al. (2025)).

On the test set, the model achieved a Dice score of 0.671 at the validation-selected threshold of 0.55, increasing to 0.83 and 0.85 with one- and two-pixel boundary tolerances, respectively. This performance is comparable to contrail detectors trained and evaluated on GOES imagery (Ortiz et al., 2025; Ng et al., 2024). Performance, however, showed a marked dependence on satellite viewing geometry. Recall was 0.855 at VZA 30–40°, remained near 0.70 between 40–60°, and decreased to 0.494 at 60–70° and 0.097 at 70–80°, while precision remained comparatively stable (0.629–0.695), indicating an increase in missed rather than false detections with viewing angle. Detection was lower over land than ocean, with recall of 0.579 versus 0.704 and Dice scores of 0.621 versus 0.683, while precision was similar (0.668 versus 0.663). Dependence on solar illumination was weaker and non-monotonic.

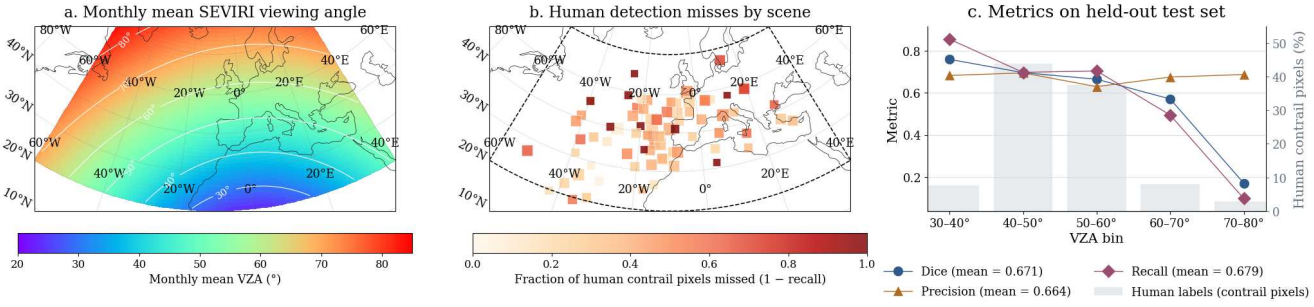


Figure 1. The satellite viewing zenith angle (VZA) across the scene pixels is shown in (a), while (b) presents the contrail detection model performance in terms of missed detections $(1 - \text{recall})$ for each MSG-SEVIRI test scene. No clear longitudinal dependence is observed, although a higher number of missed detections appears toward the upper-left corner of the domain, where VZAs are largest.

3.1.1 Contrail cover and traffic-related metrics

For each satellite snapshot t, the percentage of regional area covered by detected contrails at probability threshold P is calculated as

$$C_{r,t}(P) = \frac{100}{A_r} \sum_{i \in r} A_i d_{i,t}(P), \tag{1}$$

where A_i is the physical pixel area, A_r is the total regional area, and $d_{i,t}(P)$ is the binary detection mask at threshold P. Central estimates use $P = 0.55$, which maximizes the validation-set Dice score, while $P = 0.05$ and $P = 0.95$ provide higher and lower coverage estimates to assess detection sensitivity (supplementary Section 2).

To compare contrail coverage relative to air traffic across subregions, we calculate the accumulated detected contrail area per unit cruise distance:

$$Q_r = \frac{\sum_t \sum_{i \in r} A_i d_{i,t}(P)}{D_r}, \tag{2}$$

where D_r is the total annual cruise distance within region r. The metric is expressed in $\mathrm{m^2\,m^{-1}}$.

To visualize contrail coverage relative to cruise distance in Figure 3(c), we define the following dimensionless index:

$$M_i = \frac{C_i / \overline{C}}{D_i / \overline{D}}, \tag{3}$$

where C_i and D_i are the annual mean contrail coverage and total cruise distance in grid cell i, respectively, and the overbars denote spatial means.

3.2 Cloud property retrieval

Cloud properties required for the radiative forcing calculations were initially obtained from the Optimal Cloud Analysis (OCA) product provided by EUMETSAT for MSG-SEVIRI observations. OCA is a cloud retrieval algorithm designed to characterize a broad range of cloud types, retrieving properties for up to two overlapping layers, including cloud-top pressure, optical depth, and effective radius, using an optimal-estimation framework applied to visible and infrared SEVIRI observations (Bozzo et al., 2024). The retrieval iteratively minimizes differences between observed radiances and those simulated by a fast forward radiative-transfer model. Each cloud layer is represented as vertically homogeneous and geometrically infinitesimal, with a single microphysical phase and optical depth defined at 0.55 μm, as described in greater detail by Watts et al. (2011). Although OCA is designed to retrieve properties across different cloud types, validation against independent lidar-based observations has shown better performance for low- and mid-level clouds, with substantially larger biases in optical depth and effective radius for high-altitude ice clouds (Bozzo et al., 2024), which are the focus of this study.

To address these limitations, an empirical calibration model (Section 3.2.1) was developed to adjust OCA-derived properties of single-layer and upper-layer ice clouds when we have two-layer of clouds towards retrievals from the Cirrus Properties from SEVIRI (CiPS) algorithm (Strandgren et al., 2017a). CiPS employs artificial neural networks trained on collocated SEVIRI thermal infrared observations and cloud products from the Cloud-Aerosol Lidar with Orthogonal Polarization (CALIOP), together with auxiliary meteorological information. By exploiting the sensitivity of lidar measurements to optically thin cirrus, CiPS enables retrievals at 15-minute intervals during both day and night, providing cirrus detection and opacity probabilities, cloud-top height, ice optical depth, and ice water path. Unlike OCA, CiPS was specifically developed for cirrus cloud detection and characterization, and its performance has been extensively evaluated against independent observations across different surface types, vertical cloud configurations, and optical depth ranges (Strandgren et al., 2017b), motivating the use of CiPS retrievals as a reference for calibrating contrail properties. Therefore, in this work, native OCA retrievals were only kept for cloud-phase identification and characterization of underlying low-level clouds in multilayer cases.

3.2.1 Empirical regression-based calibration of contrail properties

CiPS retrievals provided alongside the MSG contrail dataset (Section 2.3) were used as an empirical reference to derive a multivariate linear calibration for OCA upper-layer cloud-top height (CTH) (derived from cloud-top pressure using the US Standard Atmosphere as in (Dimitropoulou et al., 2026)), cloud optical depth (COD), and cloud effective radius (CER), while preserving the original OCA layer classification and lower-layer properties. The correction was fitted at the pixel level using paired OCA–CiPS retrievals on contrail detections. For each paired pixel, the predictor vector is

$$\mathbf{x}_i = [1, \mathrm{CTH}_{\mathrm{OCA}}, \mathrm{COD}_{\mathrm{OCA}}, \mathrm{CER}_{\mathrm{OCA}}, \mathbf{R}_{\mathrm{SEVIRI}}, \mathrm{layer}_{\mathrm{OCA}}, F_{\mathrm{land}}, \mathrm{VZA}, \mathrm{SZA}], \qquad \mathbf{x}_i \in \mathbb{R}^{19}, \tag{4}$$

where $\mathbf{R}_{\mathrm{SEVIRI}}$ contains the 11 SEVIRI channels from VIS006 to IR134 (excluding the HRV band), $\mathrm{layer}_{\mathrm{OCA}}$ is a binary single-/multilayer indicator, and F_{land} is a binary land/ocean indicator. For each target property $p \in \{\mathrm{CTH}, \mathrm{COD}, \mathrm{CER}\}$, an independent ridge-regression model was fitted between the CiPS reference values and the predictor set. Ridge regression extends ordinary least squares with an L_2 penalty on the regression coefficients (Hoerl and Kennard, 1970), reducing sensitivity to collinearity among the OCA variables and SEVIRI channels. For each property p, the target $z_i^{(p)}$ is the corresponding CiPS reference value. To reduce heteroscedasticity, COD and CER targets were transformed to logarithmic space:

$$y_i^{(p)} = \begin{cases} \log z_i^{(p)}, & p \in \{\mathrm{COD}, \mathrm{CER}\}, \\ z_i^{(p)}, & p = \mathrm{CTH}. \end{cases} \tag{5}$$

The predictors were standardized using the training-set mean μ_j and standard deviation σ_j as $x_{ij,s} = (x_{ij} - \mu_j)/\sigma_j$ for each predictor $j > 0$ (i.e., except the intercept). The resulting matrix $X_s \in \mathbb{R}^{n \times 19}$ contains one row per paired contrail pixel, with the first column set to 1 for the intercept and the remaining 18 columns containing the standardized predictors. The model coefficients for each cloud property were estimated by minimizing

$$\widehat{\boldsymbol{\beta}}^{(p)} = \arg\min_{\boldsymbol{\beta}} \left[\left\| \mathbf{y}^{(p)} - X_s \boldsymbol{\beta} \right\|_2^2 + \alpha \left\| \boldsymbol{\beta}_{\mathbf{1}:} \right\|_2^2 \right], \tag{6}$$

where $\alpha = 10$ controls the regularization strength and was selected based on validation performance. $\boldsymbol{\beta}_{\mathbf{1:}} \in \mathbb{R}^{18}$ is the coefficient vector without the intercept. The intercept was left unpenalized because, after standardizing the predictors to zero mean, it represents the baseline level of the target rather than the contribution of any predictor; penalizing it would therefore bias the overall fitted level toward zero. Final models were then fitted using all valid paired pixels. For a new OCA pixel, the standardized predictor vector $\mathbf{x}_{i,s}$ was used to obtain

$$\widehat{y}^{(p)} = \widehat{\beta}_0^{(p)} + \mathbf{x}_{i,s}^{\mathsf{T}} \widehat{\boldsymbol{\beta}}^{(p)}, \tag{7}$$

where $\widehat{\beta}_0^{(p)}$ is the fitted intercept and $\widehat{\boldsymbol{\beta}}^{(p)}$ the ridge-regression coefficient vector for property p. For the case of COD and CER predictions, they are subsequently transformed back to linear space.

Model performance was evaluated using the scene-held-out split described in Table 1, ensuring that pixels from the same scene were not shared between training and test sets. Agreement between the fitted OCA properties and the CiPS reference, together with their corresponding distributions, is shown in Figure 2. Strong linear correlations were obtained for optical depth and effective radius ($r > 0.9$), while cloud-top height showed a weaker correlation ($r \approx 0.56$) but an RMSE below 0.9 km. Beyond the pixel-wise correlation, the fitted retrievals reproduce the CiPS property distributions substantially better than the native OCA values, which showed strong systematic biases (supplementary Section 3.1). This distributional agreement is particularly important for the subsequent radiative-forcing calculations, as biased cloud-property distributions can propagate directly into the radiative forcing estimates (a comparison is provided in Suppementary Section 3.2).

Table 1. Training and test split of the manually labeled contrail pixels used to fit OCA pixel-level cloud properties to the corresponding CiPS retrievals, based on the dataset of Santos Gabriel et al. (2026).

Split	Scenes	Pixels	Land	Ocean	OCA single layer	OCA multi-layer
Train	69 (80.2%)	31,047 (79.9%)	7,682 (24.7%)	23,365 (75.3%)	21,999 (70.9%)	9,048 (29.1%)
Validation/Test	17 (19.8%)	7,821 (20.1%)	1,076 (13.8%)	6,745 (86.2%)	5,746 (73.5%)	2,075 (26.5%)
Total	86 (100%)	38,868 (100%)	8,758 (22.5%)	30,110 (77.5%)	27,745 (71.4%)	11,123 (28.6%)

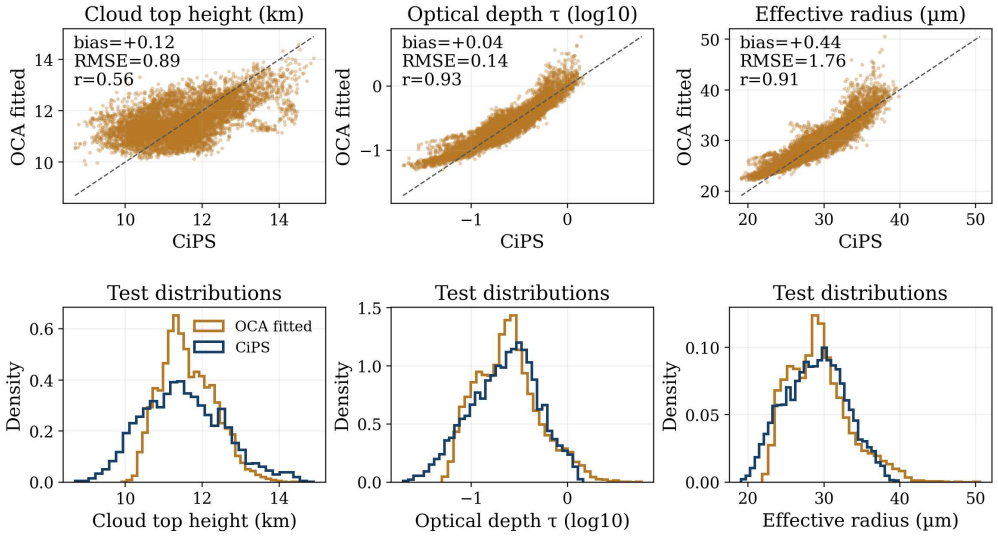


Figure 2. Comparison of fitted OCA retrievals with the CiPS reference retrievals for cloud-top height, optical depth, and effective radius on the held-out test set of human-labeled SEVIRI images. Upper panels show pixel-wise scatterplots with the 1:1 reference line, with annotations reporting bias, RMSE, and Pearson correlation. Lower panels show the corresponding fitted-OCA and CiPS distributions. Optical depth is expressed as $\log_{10}(\tau)$.

3.3 Radiative forcing estimation

The shortwave and longwave radiative forcing of each detected contrail pixel is estimated through multidimensional interpolation of radiative forcing look-up tables developed by Dimitropoulou et al. (2026). The interpolation combines SEVIRI L2 cloud properties from the OCA product together with solar zenith angle, surface spectral albedo from the International Geosphere Biosphere Program (IGBP) library, and skin temperature from ECMWF Numerical Weather Prediction data (ECMWF, 2019). They were designed to avoid the computational cost of running radiative transfer simulations for every pixel in geostationary imagery and were specifically developed for high-altitude ice clouds observed by MSG/SEVIRI. Validation against collocated CERES observations, with an approximately 20-km equivalent nadir footprint, yielded correlation coefficients of 0.86 for longwave fluxes and 0.99 for shortwave fluxes. In this study, the lookup tables are applied using the calibrated contrail cloud properties and the original OCA retrievals for underlying cloud layers, as described in Section 3.2.1.

3.3.1 Pixel-level and region-normalized metrics

The shortwave and shortwave radiative forcing at each pixel i, expressed in $\mathrm{W\,m^{-2}}$, are computed following Dimitropoulou et al. (2026) as

$$\begin{aligned} SW_i &= F^{\mathrm{sol}}_{i,\mathrm{c}} - F^{\mathrm{sol}}_{i,\bar{\mathrm{c}}} = \left[F^{\mathrm{sol}}_{\downarrow} - F^{\mathrm{sol}}_{\uparrow}\right]_{i,\mathrm{c}} - \left[F^{\mathrm{sol}}_{\downarrow} - F^{\mathrm{sol}}_{\uparrow}\right]_{i,\bar{\mathrm{c}}}, \\ LW_i &= F^{\mathrm{tir}}_{i,\mathrm{c}} - F^{\mathrm{tir}}_{i,\bar{\mathrm{c}}} = \left[F^{\mathrm{tir}}_{\downarrow} - F^{\mathrm{tir}}_{\uparrow}\right]_{i,\mathrm{c}} - \left[F^{\mathrm{tir}}_{\downarrow} - F^{\mathrm{tir}}_{\uparrow}\right]_{i,\bar{\mathrm{c}}}. \end{aligned} \tag{8}$$

where F_i^{sol} and F_i^{tir} denote the solar and thermal infrared fluxes, respectively, and the subscripts c and $\bar{\mathrm{c}}$ refer to fluxes computed with and without the contrail. The net radiative forcing at pixel i is then defined as $RF_i = LW_i + SW_i$ with positive (negative) values indicating warming (cooling).

The regional mean radiative forcing, expressed in $\mathrm{mW\,m^{-2}}$, is calculated for each satellite snapshot t as

$$RF_{r,t}(P) = \frac{1}{A_r} \sum_{i \in r} RF_{i,t}\, A_i\, d_{i,t}(P), \tag{9}$$

where $RF_{i,t}$ is the pixel-level radiative forcing, A_i is the physical pixel area, A_r is the total geographical area of region r, and $d_{i,t}(P)$ is the binary contrail detection mask at probability threshold P.

The contribution of each subregion to the domain-wide annual net warming is calculated by weighting its mean net radiative forcing by its geographical area, accounting for differences in subregion size. The percentage contribution is given by

$$f_{\mathrm{NET},r} = 100\, \frac{A_r\, \overline{F}_{\mathrm{NET},r}}{A_t\, \overline{F}_{\mathrm{NET},t}}, \tag{10}$$

where A_r and $\overline{F}_{\mathrm{NET},r}$ are the area and annual mean net radiative forcing of subregion r, respectively, while A_t and $\overline{F}_{\mathrm{NET},t}$ represent the corresponding values for the entire Euro–Atlantic domain.

4 Results

The geographical, diurnal, and seasonal variability of detected contrail coverage is examined in Sections 4.1, 4.2, and 4.3, respectively. Sections 4.4 and 4.5 investigate the retrieved cloud properties following CiPS calibration, focusing on land–ocean differences and the influence of cloud layering and day–night conditions on radiative forcing. Finally, area-normalized radiative forcing is assessed for the entire study domain in Section 4.6 and for individual subregions in Section 4.7, reflecting the combined influence of contrail coverage, cloud properties, and regional extent.

4.1 Geographical distribution of the detected contrail coverage

For the geographical analysis, six main subregions were defined using geographical bounding boxes to facilitate comparisons of regional air traffic, meteorological conditions, and surface background effects. These regions are illustrated in Figure 3(c), with their exact geographical boundaries provided in supplementary Table S1.

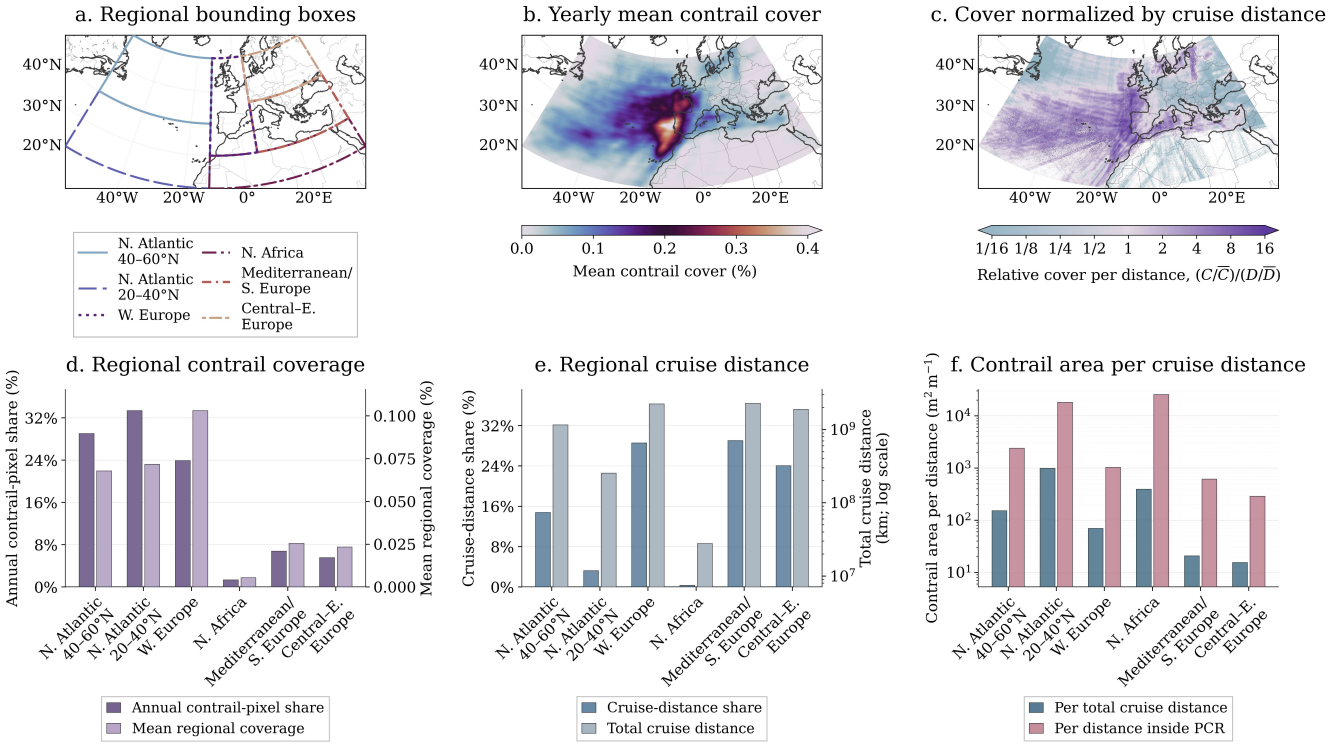


Figure 3. Contrail cover and cruise traffic over the North Atlantic, Europe and North Africa in 2023, using CoaT detections at probability ≥0.55. (a) Six regional analysis boxes. (b) Mean detected contrail cover. (c) Relative cover per cruise distance, $(C/\bar{C})/(D/\bar{D})$, where C is mean grid-cell cover and D is annual grid-cell cruise distance; reference means use the same retained cells. The index is displayed on a logarithmic colour scale from $1/16$ to 16, where 1 represents the domain reference, and 2 and $1/2$ indicate twice and half the reference coverage per unit distance, respectively. (d) Regional shares of accumulated detected contrail pixels and area-weighted mean regional coverage. (e) Regional shares and totals of cruise distance. (f) Accumulated detected contrail area per total cruise distance and per distance inside PCR, defined by satisfaction of the Schmidt–Appleman criterion and corrected ice-relative humidity ≥100%. Distance totals in (e) and ratios in (f) use logarithmic scales. Numerical values are provided in Table S1.

The annual results reveal a strong concentration of contrail detections over the North Atlantic Ocean, evident in both the annual coverage map (Figure 3(b)) and the monthly averages (Figure 4). This region accounts for nearly 76% of all annual detections, with 62% occurring within the two defined North Atlantic subregions and a further 14% over the Atlantic waters included in the Western Europe subregion (supplementary Table S4). This distribution reflects the strong contribution of long-haul transatlantic traffic across the North Atlantic and its adjacent European entry and exit corridors to the occurrence of large, persistent contrails detectable by SEVIRI. Within the North Atlantic, however, a clear latitudinal contrast emerges (Figure 3(c)). Although the North Atlantic region south of 40°N accounts for only about 22% of the cruise distance flown farther north, it contributes approximately 15% more detected contrail pixels and has about 6.5 times as much accumulated contrail area per unit cruise distance (992 compared with 152 $m^2\,m^{-1}$). Part of this contrast, however, likely arises from ob-

servational effects, as the larger viewing angles at higher latitudes toward the edges of the disk (Figure 1) reduce the effective spatial resolution of SEVIRI and consequently the detectability of contrails. A comparison with higher-resolution Visual Infrared Imaging Radiometer Suite (VIIRS) observations over part of the same 2023 period comfirms this limitation, revealing substantially more detections between $50°$N and $60°$N than are captured by SEVIRI (supplementary Section 5). Nevertheless, the longitudinal distribution of contrails observed by VIIRS broadly agrees with that of SEVIRI, with contrail coverage predominantly concentrated over the North Atlantic and extending towards Western Europe across most seasons. Both sensors also capture increased coverage in the eastern part of the domain during autumn (further discussed in Section 4.3), supporting the conclusion that the observed west–east contrast is not merely an artefact of SEVIRI's coarser spatial resolution.

In contrast with the Atlantic, central–eastern Europe and the region containing southern Europe and the Mediterranean contribute only $\sim 6\%$ and $\sim 7\%$ of annual detected contrail coverage, despite together accounting for $\sim 55\%$ of cruise distance flown in the study region. Accordingly, their coverage per unit distance is among the lowest, at 15 and $20\ \mathrm{m^2 m^{-1}}$, respectively. The particularly low contrail coverage over Eastern Europe may partly reflect the airspace closures and restrictions associated with the war in Ukraine, which reduced available European airspace by approximately 20% during 2023 and altered regional traffic patterns (EUROCONTROL, 2024). Nevertheless, the substantial cruise distance recorded within the defined regional boundaries (Figure 3(e)) and also the substantial fraction of it occuring in persistent contrail forming regions according to meteorological data (Figure 3(d) and Table S4) suggests that differences in traffic volume alone are unlikely to explain the low detected coverage over Europe. Other factors may contribute, including reduced detectability over heterogeneous land backgrounds (Mannstein et al., 1999), where thin contrails may potentially require greater optical depths to be distinguished in thermal infrared imagery over continental regions (Duda et al., 2023). However, substantially lower contrail coverage per unit distance flown than compared with the North Atlantic is observed not only over eastern continental Europe, but also over other water-covered regions, including the Black Sea ($1.6\ \mathrm{m^2 m^{-1}}$), the Baltic Sea ($8.3\ \mathrm{m^2 m^{-1}}$), and the Mediterranean Sea ($9\ \mathrm{m^2 m^{-1}}$). This suggests that the west–east contrast in detected contrail coverage cannot be explained by differences in ocean-surface detectability alone, but may also reflect a combination of meteorological conditions favoring contrail persistence and spreading over the North Atlantic.

Irvine et al. (2012) investigated the distribution of ice-supersaturated regions under different weather regimes, finding frequent enhanced occurrence south of the jet stream. Given that eastbound transatlantic flights are often routed within or close to the jet to benefit from strong tailwinds and reduce flight time and fuel consumption (Laken et al., 2012), and that traffic is concentrated along established flight corridors, these routes may be more likely to encounter atmospheric conditions favourable for contrail persistence, potentially contributing to the higher observed coverage over the North Atlantic. This interpretation is also consistent with an earlier satellite-based study by DeGrand et al. (2000) over the United States and adjacent regions, which found that contrails were frequently associated with jet streams and frontal systems, often coexisting with other clouds, including natural cirrus. Figure 4 illustrates the monthly variability in the spatial distribution of detected contrails throughout 2023, with most months showing the highest concentrations towards the westernmost longitudes of the domain. However, the

relationship between contrail locations and the jet-stream axis is difficult to resolve from monthly averages, as the jet position varies considerably from day to day. Shorter averaging periods, such as one week, may better preserve this spatial relationship and reveal the influence of atmospheric circulation on detected contrail cover, as illustrated in supplementary Figure S8.

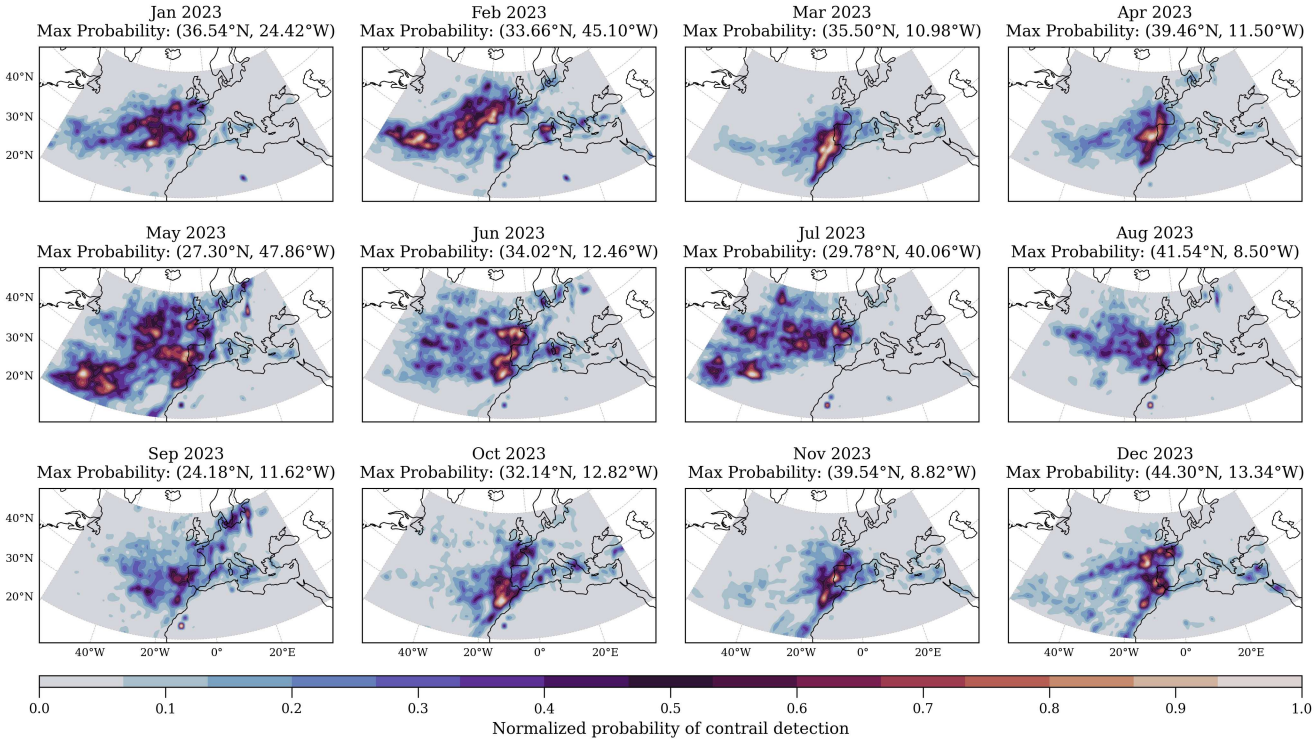


Figure 4. Monthly maps of contrail detection probability derived from MSG/SEVIRI observations detections over the Euro–Atlantic domain (60°W–40°E, 20°N–60°N) in 2023. The changing coordinates of the maximum detection probability are reported in each panel subtitle.

Beyond the North Atlantic, western Europe accounts for a substantial fraction ($\sim 24\%$) of the total detected contrail coverage, encompassing the Iberian Peninsula, France, the British Isles, the portion of North Africa north of 30°N within the same longitudinal sector, and adjacent waters (supplementary Table S1). Relative to its geographical extent, this region has the highest mean contrail coverage, with detected contrails covering approximately 0.103% of its total area (Figure 3(d)), and remaining high across the year (Figure 4). Its contrail-covered area per unit distance flown is nonetheless lower than over the North Atlantic because air traffic is considerably denser, with a mean value of $99 \mathrm{m}^2, \mathrm{m}^{-1}$. High concentrations of detected contrails over western Europe have also been reported in previous MSG/SEVIRI studies. Vázquez-Navarro et al. (2015) identified maxima west of the Iberian Peninsula and along routes towards South America, while Dekoutsidis et al. (2023) highlighted western Europe and adjacent Atlantic regions as major detection hotspots. This concentration may also partly reflect eastward advection of persistent contrails formed along North Atlantic flight corridors into western Europe (Burkhardt and Kärcher, 2011).

Contrail coverage over North Africa accounts for approximately 1.33% of the annual total, despite the region containing only 0.4% of the total cruise distance. Consequently, the contrail-covered area normalized by distance flown is among the highest of all regions, reaching about $393\ \mathrm{m}^2, \mathrm{m}^{-1}$ when normalized by total cruise distance and increasing further when only distance flown within persistent contrail-forming regions is considered, since such favorable conditions occur more rarely over the desert. Nevertheless, because North Africa lies at lower latitudes than central–eastern Europe, differences in satellite viewing geometry may also bias higher the coverage in this region because of better detectability compared to other regions.

4.2 Diurnal coverage and air traffic patterns across regions

Diurnal patterns are analyzed in relation to air traffic schedules in Figure 5. Because traffic patterns vary geographically, the analysis is presented separately for the regions defined in Figure 3. Air traffic is represented by total cruise distance flown (here defined as distance flown above 8 km altitude, similar to Meijer et al. (2022)). Although the analysis could have been restricted to flights crossing persistent contrail-forming regions, applying this restriction mainly reduced the magnitude of the distance flown without consistently altering its diurnal pattern. The results show that the relationship between traffic and detected contrail coverage is strongly region dependent. Over the North Atlantic, contrail coverage exhibits two comparable maxima, with mean values of approximately 0.091% during both the 04:00–06:00 UTC and 14:00–16:00 UTC periods. The absolute maximum is 0.101% at 14:00 UTC (Figure 5a,b). Thus, the North Atlantic signal is better described as a clear bimodal cycle than as a single dominant morning maximum. This agrees with the eastbound–westbound interpretation reported by Graf et al. (2012): the early-morning enhancement is consistent with eastbound flights departing North America during the previous evening, whereas the afternoon enhancement is consistent with westbound traffic departing Europe during the late morning. The contrast is much stronger over Europe. In western Europe, coverage rises from a daily minimum of 0.055% at 01:00–02:00 UTC to a maximum of 0.213% at 07:45 UTC. The 06:00–08:00 UTC mean is 0.194%, compared with 0.090% during 14:00–17:00 UTC, giving a morning-to-afternoon ratio of 2.16. The corresponding ratios are 1.98 in the Mediterranean–southern Europe and 2.82 in central–eastern Europe. Similar single morning maxima have been reported in contrail-detection studies over the continental United States using both geostationary observations (Meijer et al., 2022) and polar-orbiting satellite observations (Palikonda et al., 2005), with morning contrail coverage reaching nearly twice the afternoon value, consistent with the findings of the present study. One explanation proposed by Palikonda et al. (2005) is that early-morning conditions may favour the detection of newly formed linear contrails due to the reduced presence of residual cirrus from preceding hours. This mechanism could also contribute to the patterns observed here, particularly given the substantially lower nighttime flight activity compared with early morning, averaging 82% less in western Europe, 47% less in Mediterranean–southern Europe, and 73% less in central–eastern Europe during 2023, limiting the accumulation of contrail cirrus overnight. Conversely, as flight activity increases throughout the day, the accumulation and spreading of persistent contrails may contribute to a denser cirrus background, making individual linear features increasingly difficult to distinguish as the afternoon approaches. North Africa exhibits a later morning maximum, reaching only 0.010% at approximately 10:00ŨTC. Its peak coverage is about 21 times lower than in western Europe, 10 times lower than over the North Atlantic, and roughly 5 times lower than in the other

European subregions (central–eastern Europe and Mediterranean/southern Europe). This weak detected signal requires caution when interpreting the diurnal pattern in this region, which may be more sensitive to sampling variability and spatial differences in air traffic.

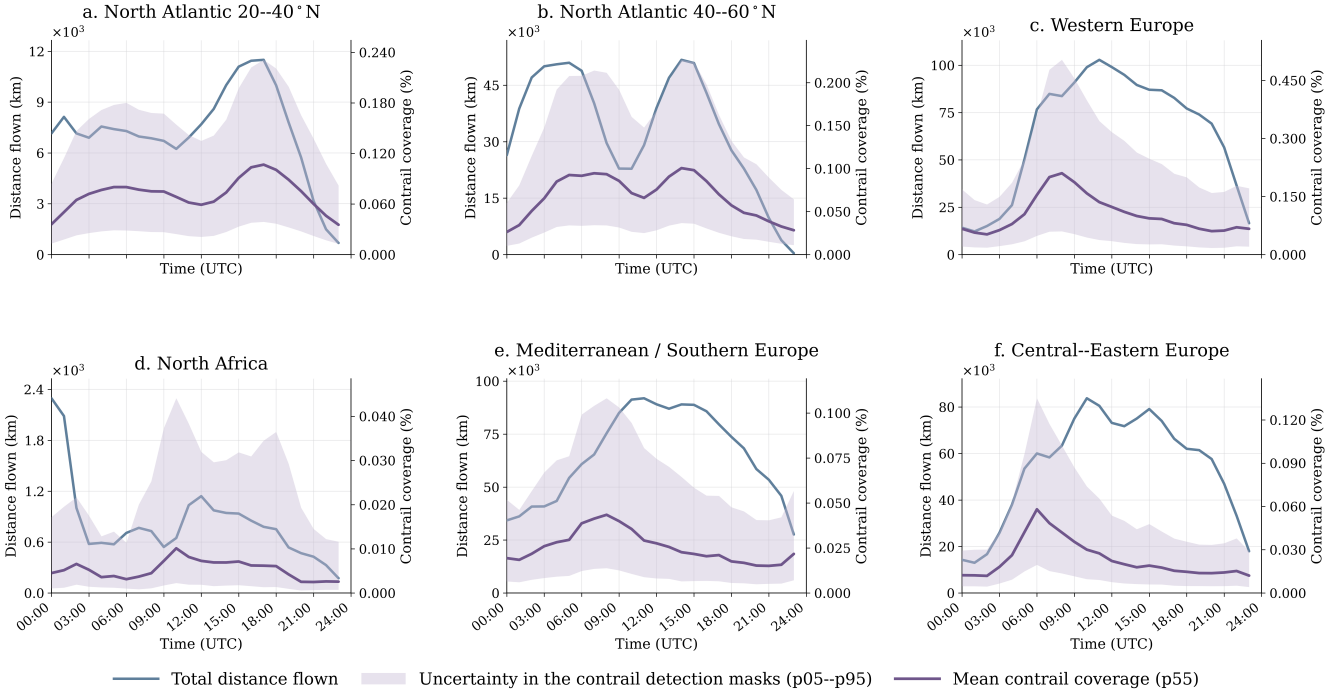


Figure 5. Diurnal cycle of satellite-derived contrail coverage and ADS-B-based cruise distance flown across the different regions of the study area. Coordinated Universal Time (UTC) is used throughout to facilitate comparison with air-traffic schedules. Mean contrail coverage is computed using the probability threshold that maximizes the Dice score on the validation set. The shaded range represents detection-threshold uncertainty, bounded by the coverage obtained using the thresholds that maximize recall (upper bound; more detections) and precision (lower bound; fewer detections) while maintaining similar Dice Score, as described in Section 3.1.

4.3 Seasonal contrail coverage variability

Monthly and seasonal variability is examined, although interannual changes in meteorological conditions may lead to different contrail coverage patterns from year to year (Teoh et al., 2022). Therefore, the observed trends reported here should be considered representative of 2023 rather than interpreted as long-term climatological patterns.

4.3.1 Contrail coverage patterns across months and regions and their relationship with air traffic

Contrail coverage over the Euro–Atlantic region exhibits a seasonal cycle (Figure 6(a)). Averaging the monthly values, mean coverage increases from 0.042% in winter (DJF: December–January–February) to 0.077% in spring (MAM: March–April–May), approximately 83% higher than the winter mean, before decreasing to 0.048% in summer (JJA: June–July–August)

and 0.045% in autumn (SON: September–October–November). At the monthly scale, coverage reaches its maximum in May (0.084%) and its minimum in December (0.031%). A similar spring maximum in contrail occurrence has been reported in previous observational studies (Meijer et al., 2022; Minnis et al., 2005).

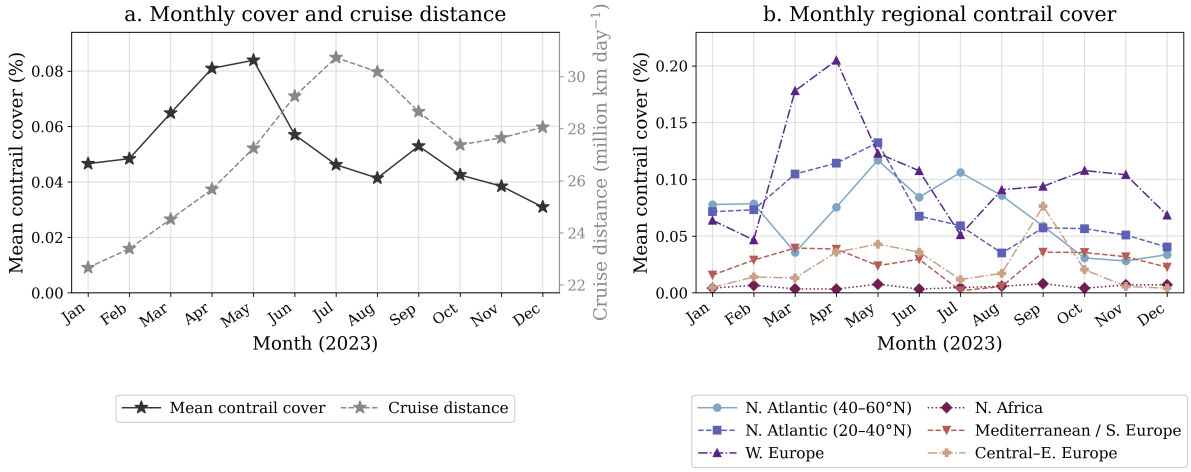


Figure 6. Monthly variations in contrail cover and cruise distance during 2023. (a) Full-domain monthly mean contrail cover (left axis, solid dark gray) and monthly mean daily cruise distance (right axis, dashed light gray). (b) Monthly mean contrail cover within the six regional boxes. Detection masks are binarized at $p \geq 0.55$ over 20–60°N and 60°W–40°E. For each snapshot, cover is the detected physical pixel area divided by the full physical area of the domain or subregion, then averaged equally over snapshots within each month. Cruise distance retains the existing aircraft data and excludes daily distances below 80% of the corresponding monthly median.

The regional analysis in Figure 6(b) shows that seasonal variability in contrail coverage is not spatially uniform. Western Europe exhibits the highest annual mean coverage (0.103%) and the largest seasonal variation in absolute terms. Mean coverage increases from 0.060% in winter to 0.169% in spring, a factor of approximately 2.8, with a monthly maximum of 0.205% in April, before decreasing by approximately 51% to 0.083% in summer. The North Atlantic shows a different seasonal structure, with a marked contrast between the regions north and south of 40°N. South of 40°N, mean coverage decreases from 0.117% in spring to 0.054% in summer, a reduction of approximately 54%. North of 40°N, summer coverage remains high in summer, averaging 0.092% and reaching 0.106% in July, close to its annual monthly maximum of 0.117% in May. This contrasting behaviour is consistent with the climatological poleward migration of the North Atlantic jet stream during summer (Hallam et al., 2022; DeGrand et al., 2000) (see supplemantary Figure S8), which also favours a northward shift in transatlantic flight routes, potentially explaining why summer coverage remains high at northern latitudes while declining farther south (see also Figure 7(a)).

The regional differences are also substantial in terms of annual mean coverage. Western European coverage is approximately 1.2–1.6 times higher than over the North Atlantic, around four times higher than over the Mediterranean and Central–Eastern Europe, and more than an order of magnitude higher than over North Africa. These contrasts indicate that the domain-wide

seasonal signal is not produced by a uniform increase in contrail occurrence across the study area. Instead, the pronounced spring maximum is largely associated with the strong increase over Western Europe, which contains the largest concentration of detections, while the North Atlantic exhibits a distinct latitudinal redistribution and the remaining regions contribute comparatively little to the domain-wide variability.

Unlike the diurnal patterns, which closely follow air traffic schedules, monthly contrail coverage shows little correspondence with traffic (Figure 6(a)). Mean cruise distance increases from 24.70 million km day^{-1} in winter to 25.81 in spring and 30.05 in summer. Thus, summer traffic is approximately 16% higher than spring traffic, while detected contrail coverage is 37% lower. This weak monthly relationship (Pearson's $r \approx -0.23$) suggests that the observed seasonal distribution is not primarily driven by air traffic volume, but is strongly influenced by atmospheric circulation and meteorological conditions affecting contrail persistence, growth, and satellite detectability.

4.3.2 Variability in contrail coverage with geographical, diurnal and satellite observation conditions

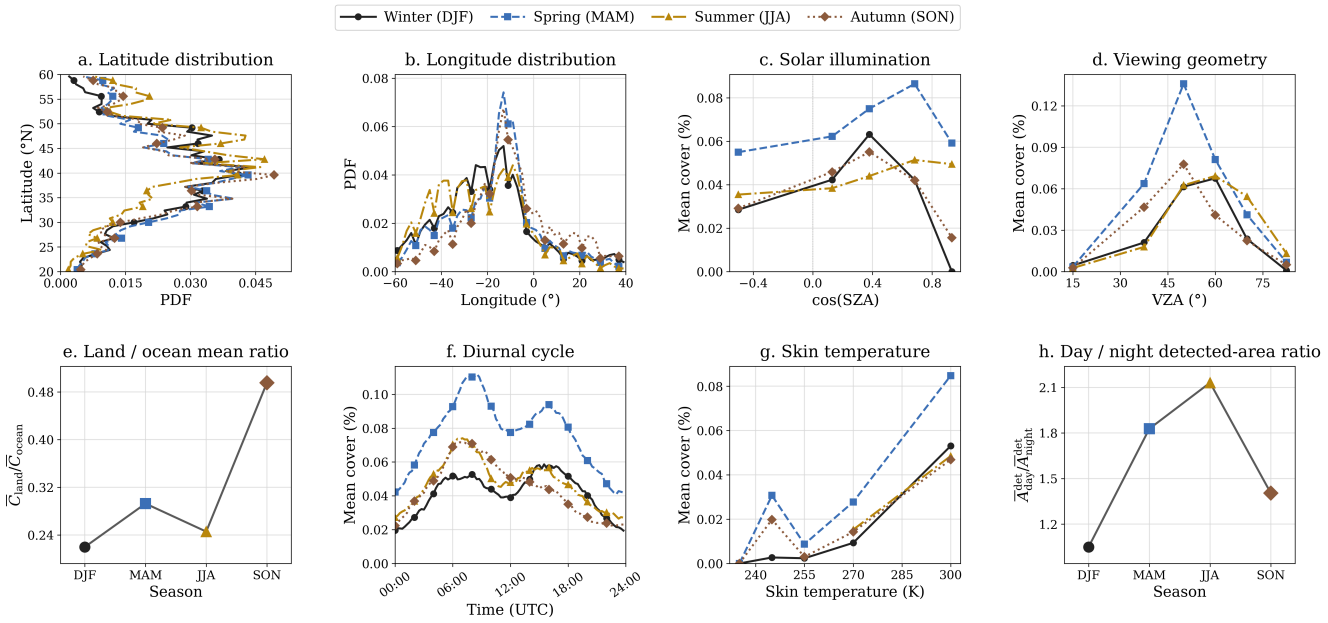


Figure 7. Seasonal distributions and mean detected contrail coverage over the Euro–Atlantic domain (60°W–40°E, 20–60°N) in 2023. Colors and markers distinguish winter (DJF), spring (MAM), summer (JJA), and autumn (SON). Panels show (a) latitude and (b) longitude probability density functions (PDF) of detected contrail pixels; mean coverage as a function of (c) solar illumination, expressed as cos(SZA), and (d) viewing zenith angle (VZA); (e) the ratio of mean coverage over land to that over ocean; (f) the diurnal coverage cycle in UTC; (g) coverage across skin-temperature bins; and (h) the ratio of daytime to nighttime mean coverage. Detections use detection probabilities binarized at p=0.55. For each snapshot, coverage is calculated as the detected contrail area within a conditioning class divided by the total physical area of that same class, including both detected and undetected pixels, and expressed as a percentage. Daytime corresponds to SZA$\leq 90°$ and nighttime to SZA$\geq 90°$; both ratios are calculated from seasonal means.

Figure 7 summarizes the seasonal geographical, diurnal, and observational variability of detected contrail coverage in 2023. Panels (a,b) show normalized spatial distributions of detections, while the remaining panels show physical-area-normalized mean coverage. Consistent with the previously discussed seasonal northward migration of the North Atlantic jet stream and associated contrail-forming conditions, the geographical distributions show a shift towards higher latitudes in summer, with mean detection latitude reaching $43.0°$N, compared with $40.1°$N in winter and $39.7°$N in spring. Summer detections are also more concentrated over the western Atlantic, with 73.2% occurring west of $10°$W. In autumn, the distribution shifts eastward, with the fraction of detections west of $10°$W decreasing to 55.6% and the land-to-ocean coverage ratio increasing from 0.25 in summer to 0.50 in autumn (panel e). This redistribution may also be associated with the pronounced northward displacement of the jet stream over eastern Europe during late summer and early autumn during the study year (supplementary Figure S8), potentially shifting conditions favourable for persistent contrail formation towards the continental region. The seasonal diurnal

cycles (panel f) further reflect this geographical redistribution. In autumn, coverage exhibits a pronounced morning maximum of 0.0718% at 07:45 UTC, without the secondary afternoon peak observed in other seasons. This resembles the diurnal pattern previously identified over the eastern subregions (Section 4.2), suggesting a greater continental influence on the domain-wide cycle in autumn. In contrast, the other seasons exhibit the double-peaked pattern characteristic of the North Atlantic, associated with eastbound and westbound transatlantic traffic.

The greater extent and duration of daylight in summer and spring contribute to the highest ratios of total daytime to nighttime detected area: 2.13 and 1.83, respectively (panel h). These seasons also show weaker variation in mean contrail cover across solar zenith angle classes (panel c). Regarding observational conditions, warmer skin-temperature classes generally exhibit higher detected coverage (panel g), potentially reflecting greater thermal contrast between cold contrails and the underlying radiating background, which may enhance their detectability in Ash RGB imagery (Section 2.1). Coverage also peaks at intermediate viewing zenith angles (panel d), reaching its maximum in the 45–55° VZA class during spring and autumn and in the 55–65° class during winter and summer. The lower detected coverage at small VZAs partly reflects their location over North Africa, where only 1.53% of cruise distance occurs within persistent contrail-forming regions, approximately four times less than over western Europe and the northern North Atlantic. Thus, fewer persistent contrails are expected despite more favourable viewing geometry. Conversely, at higher latitudes, conditions favour contrail persistence, but larger satellite VZAs reduce sensitivity to narrow contrails.

4.4 Contrail cloud property and radiative forcing distributions above land and ocean

Across the available 2023 observations, the calibrated cloud properties of detected contrails have annual mean cloud-top height, optical depth, and effective ice-crystal radius of 11.57km, 0.309, and $28.8\mu m$, respectively. The optical-depth distribution is however positively skewed, with a median of approximately 0.205. For multilayer cases, the underlying cloud has a mean cloud-top height of 2.34km and optical depth of 2.24.

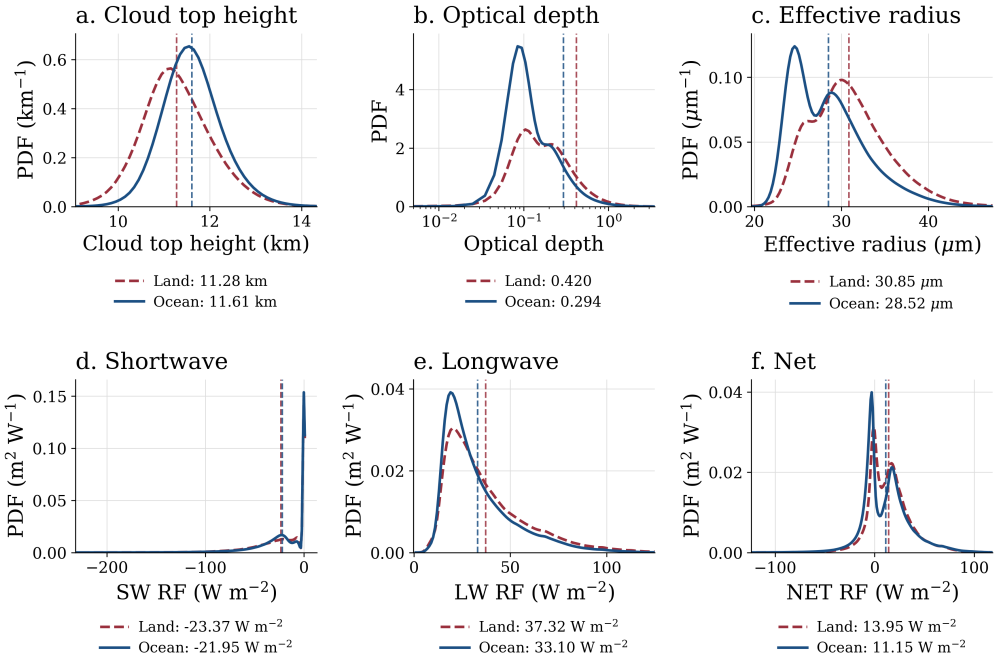


Figure 8. Yearly distributions of contrail (a) cloud-top height, (b) optical depth, (c) effective radius, and (d–f) shortwave, longwave and net radiative forcing, respectively, over land (red dashed) and ocean (blue solid). Distributions include single-layer and multilayer cases and both daytime and nighttime observations. Each distribution is normalized independently; vertical dashed lines indicate arithmetic means, whose values are given in the legends. Optical depth uses a logarithmic horizontal axis. The shortwave peak at zero includes nighttime observations. Positive and negative radiative forcing indicate warming and cooling, respectively.

Contrail properties exhibit a clear land–ocean contrast (Figure 8(a–c)), with mean optical depth approximately 43% higher over land, accompanied by slightly larger effective radii and lower cloud tops. Consistent with the interpretation of Duda et al. (2023), this contrast may partly reflect reduced detectability of optically thin contrails against heterogeneous continental infrared backgrounds, rather than necessarily indicating differences in contrail microphysical properties. Differences in sampling should also be considered, as oceanic pixels account for 88.0% of valid property observations, resulting in substantially unequal land and ocean sample sizes. The bottom row of Figure 8 presents pixel-level radiative forcing estimates, revealing differences that partly reflect the contrasting land–ocean distributions of retrieved cloud properties, with mean net forcing of $13.95\ \mathrm{W\,m^{-2}}$ over land, approximately 25% higher than the $11.15\ \mathrm{W\,m^{-2}}$ over ocean. Day–night sampling is similar over land and ocean, with nighttime observations accounting for 37.1% and 38.1% of the pixel samples, respectively. The stronger shortwave cooling and longwave warming over land therefore likely reflect its greater mean optical depth, although differences in solar illumination, atmospheric conditions, surface properties, and underlying clouds may also contribute.

4.5 Influence of cloud layering and daytime–nighttime radiative forcing

Contrail pixels detected during nighttime exhibit positive mean net radiative forcing throughout the year due to the absence of the shortwave component, ranging from 26.7 $\mathrm{W\,m^{-2}}$ in August to 37.5 $\mathrm{W\,m^{-2}}$ in December, a 40.4% increase. In contrast, detections during daytime exhibit net cooling from March through October, strongest in April (-4.4 $\mathrm{W\,m^{-2}}$), while those detected during November–January exhibit net warming, with mean forcing magnitudes representing only 12–14% of the corresponding nighttime values (Figure 9(a)).

Across all detected contrail pixels in 2023, the annual mean net radiative forcing was -1.4 $\mathrm{W\,m^{-2}}$ for daytime detections and $+32.7$ $\mathrm{W\,m^{-2}}$ for nighttime detections, with daytime cooling representing only 4.3% of the nighttime warming magnitude. As shown in Figure 9(b), cloud layering also influences these radiative effects. Contrail pixels detected during daytime exhibit mean net cooling of -5.2 $\mathrm{W\,m^{-2}}$ in single-layer cases, but net warming of $+2.3$ $\mathrm{W\,m^{-2}}$ in multilayer cases. For nighttime detections, the mean is 29.3% lower for multilayer cases ($+30.2$ $\mathrm{W\,m^{-2}}$) than for single-layer cases ($+42.7$ $\mathrm{W\,m^{-2}}$). Combining daytime and nighttime detections, mean net radiative forcing is considerably lower for single-layer cases ($+4.4$ $\mathrm{W\,m^{-2}}$) than for multilayer cases ($+15.9$ $\mathrm{W\,m^{-2}}$). This difference partly reflects the unequal day–night sampling, as nighttime observations, which exhibit substantially stronger net warming, account for only 20.0% of single-layer detections compared with 48.9% of multilayer detections.

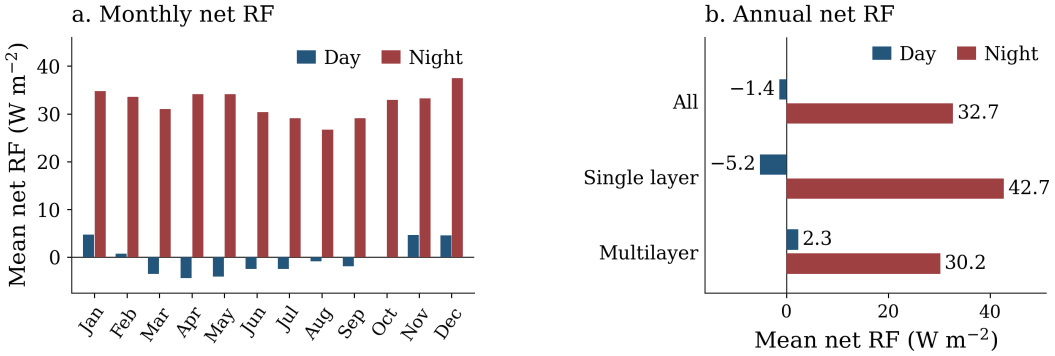


Figure 9. Mean net radiative forcing (RF) of detected contrail pixels over the Euro–Atlantic region (60°W–40°E, 20–60°N) in 2023. a. Monthly mean net RF during daytime (blue) and nighttime (red). Day and night are defined by solar zenith angles ≤90° and ≥90°, respectively. b. Annual mean net RF for all detections and separately for single-layer and multilayer cases.

4.6 Radiative forcing normalized by the study-domain area

The radiative forcing contribution of the Euro–Atlantic region, as defined in this study (60°W–40°E and 20–60°N), is calculated using Equation 9, and therefore with its magnitude depending on the geographical area considered. The results shown in Figure 10 reveal a clear seasonal cycle, with net warming remaining positive throughout 2023. Maximum net forcing occurs in January, reaching 5.01 [1.95, 10.66] mW $\mathrm{m^{-2}}$, while the minimum occurs in August at 1.35 [0.55, 2.74] mW $\mathrm{m^{-2}}$, a

factor of approximately 3.7 between the two months. These values are approximately 76% above and 53% below the annual mean, respectively. May, the month with the highest contrail coverage (Section 4.3), also exhibits the strongest longwave warming (13.69 $\mathrm{mW\,m^{-2}}$). However, greater daytime coverage during this month (Figure 7) increases shortwave cooling as well, offsetting 76% of the longwave warming and leaving a net forcing of 3.27 $\mathrm{mW\,m^{-2}}$.

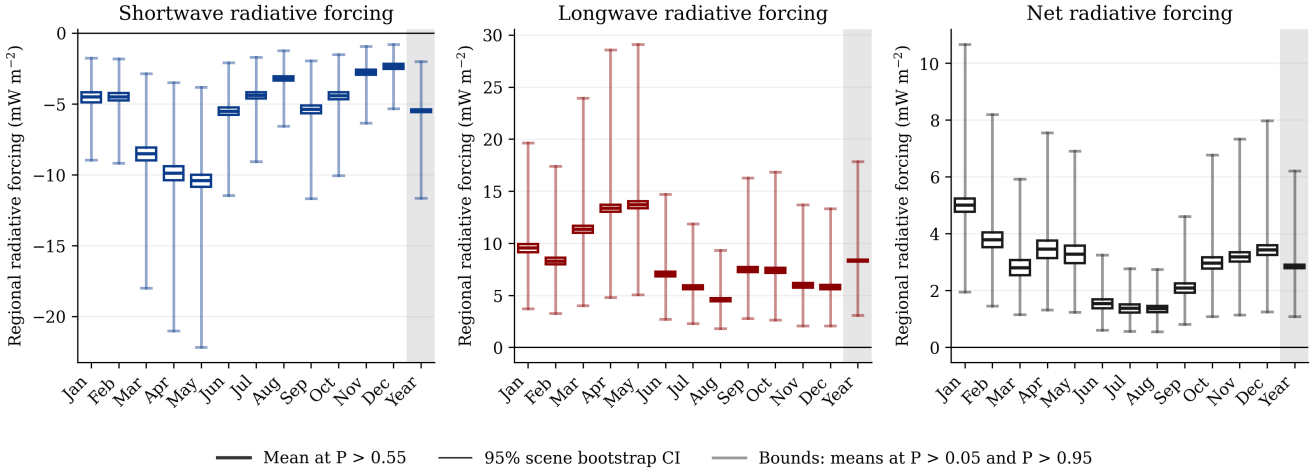


Figure 10. Monthly and annual regional contrail radiative forcing in 2023: shortwave (blue), longwave (red) and net (black), over 60°W–40°E and 20–60°N. For each scene, forcing at detected contrail pixels is weighted by pixel area and normalized by the complete regional area; all yearly scenes are then averaged with equal weights. Central lines show means at detection probability $P > 0.55$, boxes indicate 95% confidence intervals from scene-bootstrap resamples, and whiskers span the means obtained at $P > 0.05$ and $P > 0.95$, representing detection-threshold sensitivity. The shaded final column shows the annual estimate. All values are in $\mathrm{mW\,m^{-2}}$, with positive and negative forcing indicating warming and cooling, respectively.

Over the full year, mean shortwave forcing of -5.48 [-11.64, -2.00] mW $\mathrm{m^{-2}}$ partially offsets longwave warming of 8.33 [3.09, 17.85] mW $\mathrm{m^{-2}}$, yielding an annual net warming of 2.85 [1.09, 6.21] mW $\mathrm{m^{-2}}$. Thus, approximately 66% of the annual longwave warming is compensated by shortwave cooling. Although the magnitude of regional forcing is largely determined by contrail coverage, the balance between shortwave cooling and longwave warming is mostly sensitive to retrieved cloud properties, as illustrated in the supplementary Figure S5 by comparing forcing estimates derived from native and calibrated OCA retrievals.

4.7 Radiative forcing normalized by subregion areas and regional shares

The relatively low annual mean radiative forcing partly reflects the small fraction of the extensive Euro–Atlantic domain covered by detected contrails. To assess how forcing estimates depend on the geographical area considered, Table 2 presents the annual mean net forcing for the six subregions defined in this study (again following Equation 9). Western Europe, which

exhibits the highest contrail coverage, reaches a net forcing of $6.00\mathrm{mWm}^{-2}$, more than twice the domain-wide annual mean of $2.85\mathrm{mWm}^{-2}$.

Table 2. Annual mean regional net radiative forcing from detected contrails over the Euro–Atlantic domain in 2023, using the central estimates at $P > 0.55$.

Subregion	N. Atlantic 40–60°N	N. Atlantic 20–40°N	Western Europe	North Africa	Mediterranean / S. Europe	Central–Eastern Europe
Mean net RF ($\mathrm{mW\,m^{-2}}$)	4.28	3.59	6.00	0.24	1.11	0.75

Reflecting the geographical concentration of detected contrail coverage, the regional contributions to annual net warming (Equation 10) are strongly concentrated over the Atlantic (Table 3). The two North Atlantic subregions account for 65.40%, increasing to approximately 78% when including Atlantic waters within western Europe's box boundaries (supplementary Table S5). Western Europe region contributes 25.01% overall, while the remaining three subregions account for only 9.59% combined.

Table 3. Regional contributions to annual net warming from detected contrails over the Euro–Atlantic domain in 2023. Shares are calculated from annual mean net forcing at $P > 0.55$, weighted by physical regional area.

Subregion	N. Atlantic 40–60°N	N. Atlantic 20–40°N	Western Europe	North Africa	Mediterranean / S. Europe	Central–Eastern Europe
Share of net warming (%)	30.70	34.70	25.01	1.33	5.69	2.57

5 Conclusions

This study combines neural-network contrail detection in MSG/SEVIRI imagery with cloud-property retrievals and radiative-transfer lookup tables to characterize linear contrails and their radiative forcing over Europe and the North Atlantic throughout 2023. It quantifies geographical, diurnal, and seasonal variability in contrail coverage and radiative forcing, extending previous MSG-based contrail studies (Vázquez-Navarro et al., 2015; Graf et al., 2012; Wang et al., 2024; Dekoutsidis et al., 2023) by sampling detections throughout the full diurnal cycle, providing a more detailed comparison of regional patterns, and estimating shortwave and longwave forcing independently.

Results reveal a strong geographical concentration of detections over the North Atlantic, with approximately 76% occurring over Atlantic waters. Within this region, the accumulated detected contrail area per unit cruise distance is approximately 6.5 times greater south of $40°$N than farther north. This contrast may partly reflect reduced sensitivity to narrow contrails at the larger satellite viewing angles encountered at higher latitudes. Conversely, lower detected coverage over continental Europe cannot be explained by viewing geometry alone and may partly reflect reduced sensitivity to thin contrails against heterogeneous land backgrounds, consistent with the 43% higher mean optical depth observed over land than ocean. Regional

differences in contrail persistence and spreading, potentially influenced by jet-stream position, may further contribute to this contrast.

Diurnal coverage exhibits two maxima over the North Atlantic, consistent with eastbound and westbound traffic, whereas European regions show pronounced morning peaks, with morning-to-afternoon coverage ratios ranging from 1.98 in Mediterranean–southern Europe to 2.82 in central–eastern Europe. The afternoon decline may partly reflect reduced detectability against an increasingly dense cirrus background. Seasonally, domain-wide coverage peaks in spring (0.077%), approximately 83% above winter. Despite 16% greater cruise traffic in summer than in spring, detected coverage decreases by 37%, demonstrating that seasonal coverage does not simply follow traffic volume. The seasonal cycle also differs substantially between subregions, with detections shifting northward in summer and eastward in autumn, consistent with seasonal changes in jet-stream position and associated conditions favourable for persistent contrails.

Contrail detections exhibit weak mean daytime cooling but substantial nighttime warming, with net warming approximately 25% greater over land than ocean. During daytime, single-layer contrails produce net cooling, whereas multilayer cases produce net warming. Both exhibit net warming overall, although it is 3.6 times greater for multilayer cases, partly reflecting their higher proportion of nighttime detections. Normalized by the Euro–Atlantic domain area, annual net forcing is $+2.85\,\mathrm{mW\,m^{-2}}$ [1.09, $6.21\,\mathrm{mW\,m^{-2}}$], with shortwave cooling offsetting approximately 66% of longwave warming. Net forcing remains positive throughout the year, peaking in January, despite maximum detected coverage occurring in spring, and reaching its minimum in August. Geographically, the strong concentration of detected contrail coverage results in approximately 78% of annual net warming originating from Atlantic waters, highlighting the disproportionate contribution of these regions to observed contrail-induced warming relative to their air traffic volume.

Overall, these findings highlight the value of geostationary observations for assessing contrail coverage and radiative forcing across geographical and temporal scales. Despite spatial resolution limitations, the observed patterns provide valuable insights into the distribution of larger, optically thicker persistent contrails, while emphasizing the importance of meteorological conditions, satellite detectability, and air traffic in interpreting the observed regional variability.

6 Discussion and future work

The present analysis is limited to linear contrails detectable in MSG/SEVIRI imagery. Gierens and Vázquez-Navarro (2017) found that such contrails typically become detectable approximately 1.5 h after formation and remain visible for about 0.9 h. Consequently, this study captures only a subset of contrails that reach sufficiently large spatial scales and optical contrast, and only during a limited fraction of their lifetime. The resulting coverage estimates should therefore be interpreted as a lower bound on total contrail-induced cloud coverage and cannot be directly compared with model estimates representing the full contrail population. Future work should exploit higher-resolution observations, particularly from the Flexible Combined Im-

ager (FCI) aboard Meteosat Third Generation (MTG) (Holmlund et al., 2021) which covers the same study region. Compared with SEVIRI's 3 km infrared sampling and 15 min temporal resolution, FCI offers 2 km infrared sampling and 10 min full-disc observations. These improvements are expected to enable earlier detection and capture a larger fraction of smaller and shorter-lived contrails. However, neither a full year of operational MTG/FCI observations nor a labeled contrail dataset suitable for transfer learning was available when this analysis was conducted, making the extension of this methodology to MTG/FCI a priority for future work.

Another important limitation concerns the availability of cloud-property retrievals, particularly for optically thin cirrus. Existing approaches often rely on algorithms trained against collocated observations from polar-orbiting instruments (Strandgren et al., 2017a; Mayer et al., 2024; Kox et al., 2014; Meijer et al., 2024), but developing and validating such a model was beyond the scope of this study. Instead, we used existing CiPS retrievals as a reference to calibrate OCA cloud properties through multivariate linear regression. Although the calibrated retrievals reasonably reproduce the range, distributions, and variability of the reference properties across different backgrounds and solar and viewing geometries, the resulting annual dataset does not exhibit clear seasonal variations in cloud optical depth, cloud-top height, or effective radius. This limitation warrants further investigation, potentially through improved retrieval models supported by independent observations from missions such as Earth Cloud, Aerosol and Radiation Explorer (EarthCARE) (Wehr et al., 2023). Future work should also provide a more comprehensive assessment of radiative forcing uncertainty by propagating uncertainties in cloud-property retrievals and other radiative calculation inputs into the domain-averaged estimates, beyond the detection-threshold sensitivity considered here.

Finally, further improvements in contrail detection and tracking would enable a more complete characterization of contrail evolution and its associated climate impact. Training the detector on temporally consecutive, manually labeled observations could improve temporal consistency and facilitate the tracking of individual contrails throughout their observable lifetimes. Existing approaches, such as the one proposed by Sonabend-W et al. (2025) for contrails evolving into cirrus, could be evaluated for this purpose. Such development would enable estimates of contrail lifetime, cloud-property evolution, and cumulative radiative forcing, extending the present snapshot-based assessment towards a more complete characterization of contrail-induced climate effects.

Code availability. The neural network model used for contrail detection is available at https://github.com/Aircraft-Operations-Lab/ContrAI.

Data availability. Aircraft trajectory and flight information for the year 2023 were obtained from the OpenSky Network https://opensky-network.org/. The look-up tables used in this study are publicly available on Zenodo https://zenodo.org/records/14859250.

Author contributions. IO is the principal author of this work. She implemented the detection algorithm (under the supervision of JGH and MS), carried out the data analysis, and served as the primary writer of the manuscript. ED, PB, and NC developed the radiative forcing look-up tables and actively contributed to the analysis of the results. JGH, HB, and JvG participated in the handling and sharing of the data. MS is the coordinator of the project; he conceived the project idea and designed the experimental setup. All authors reviewed and approved the final manuscript.

Competing interests. The authors declare no competing financial or non-financial interests.

Acknowledgements. This study was carried out in the Department of Aerospace Engineering at Universidad Carlos III de Madrid, which has been accredited as a Unit of Excellence "María de Maeztu", a distinction awarded by the Spanish State Research Agency for the period 01/01/2026-31/12/2031. The research is part of the E-CONTRAIL project, funded by the SESAR 3 Joint Undertaking under Grant Agreement No. 101114795, as well as the CLIMATION project (reference PID2024-158160OB-C31), funded by the Spanish Ministry of Science, Innovation and Universities.

References

Bickel, M., Ponater, M., Burkhardt, U., Righi, M., and Hendricks, J.: Contrail Cirrus Climate Impact: From Radiative Forcing to Surface Temperature Change, JOURNAL OF CLIMATE, 38, 2025.

Bozzo, A., Doutriaux-Boucher, M., Jackson, J., Spezzi, L., Lattanzio, A., and Watts, P. D.: First Release of the Optimal Cloud Analysis Climate Data Record from the EUMETSAT SEVIRI Measurements 2004–2019, Remote Sensing, 16, 2989, https://doi.org/10.3390/rs16162989, 2024.

Burkhardt, U. and Kärcher, B.: Global radiative forcing from contrail cirrus, Nature Climate Change, 1, 54–58, https://doi.org/10.1038/nclimate1068, 2011.

DeGrand, J. Q., Carleton, A. M., Travis, D. J., and Lamb, P. J.: A Satellite-Based Climatic Description of Jet Aircraft Contrails and Associations with Atmospheric Conditions, 1977–79, Journal of Applied Meteorology and Climatology, 39, 1434–1459, https://doi.org/10.1175/1520-0450(2000)039<1434:ASBCDO>2.0.CO;2, 2000.

Dekoutsidis, G., Feidas, H., and Bugliaro, L.: Contrail detection on SEVIRI images and 1-year study of their physical properties and the atmospheric conditions favoring their formation over Europe, Theoretical and Applied Climatology, 151, 1931–1948, https://doi.org/10.1007/s00704-023-04357-9, 2023.

Dimitropoulou, E., de Buyl, P., and Clerbaux, N.: Satellite-based estimation of high-altitude ice cloud radiative forcing derived through a Rapid Contrail-RF Estimation Approach, Atmospheric Measurement Techniques, 19, 437–459, https://doi.org/10.5194/amt-19-437-2026, 2026.

Driver, O. G. A., Stettler, M. E. J., and Gryspeerdt, E.: Factors limiting contrail detection in satellite imagery, Atmospheric Measurement Techniques, 18, 1115–1134, https://doi.org/10.5194/amt-18-1115-2025, 2025.

Duda, D. P., Minnis, P., and Nguyen, L.: Estimates of cloud radiative forcing in contrail clusters using GOES imagery, Journal of Geophysical Research: Atmospheres, 106, 4927–4937, https://doi.org/10.1029/2000JD900393, 2001.

Duda, D. P., Minnis, P., Nguyen, L., and Palikonda, R.: A Case Study of the Development of Contrail Clusters over the Great Lakes, https://journals.ametsoc.org/view/journals/atsc/61/10/1520-0469_2004_061_1132_acsotd_2.0.co_2.xml, 2004.

Duda, D. P., Bedka, S. T., Minnis, P., Spangenberg, D., Khlopenkov, K., Chee, T., and Smith Jr., W. L.: Northern Hemisphere contrail properties derived from Terra and Aqua MODIS data for 2006 and 2012, Atmospheric Chemistry and Physics, 19, 5313–5330, https://doi.org/10.5194/acp-19-5313-2019, 2019.

Duda, D. P., Jr, W. L. S., Bedka, S., Spangenberg, D. A., Chee, T., and Minnis, P.: Impact of COVID-19-related Air Traffic Reductions on the Coverage and Radiative Effects of Linear Persistent Contrails over Conterminous United States and Surrounding Oceanic Routes, Journal of Geophysical Research: Atmospheres, 128, https://ntrs.nasa.gov/citations/20230002820, 2023.

ECMWF: ERA5 monthly averaged data on single levels from 1940 to present, https://cds.climate.copernicus.eu/datasets/reanalysis-era5-single-levels-monthly-means?tab=overview, 2019.

Euchenhofer, M. V., Prashanth, P., Parke, S. A., Eastham, S. D., and Waitz, I. A.: Contrail Observation Limitations Using Geostationary Satellites, Geophysical Research Letters, 52, e2025GL118 386, https://doi.org/10.1029/2025GL118386, _eprint: https://agupubs.onlinelibrary.wiley.com/doi/pdf/10.1029/2025GL118386, 2025.

EUMETSAT: Ash RGB Quick Guide, https://user.eumetsat.int/resources/user-guides/ash-rgb-quick-guide, 2023.

EUROCONTROL: Network Manager Annual Report 2023, https://www.eurocontrol.int/publication/network-manager-annual-report-2023, 2024.

Gierens, K. and Vázquez-Navarro, M.: Statistical analysis of contrail lifetimes from a satellite perspective, Meteorologische Zeitschrift, p. 88472, https://doi.org/10.1127/metz/2018/0888, 2017.

Graf, K., Schumann, U., Mannstein, H., and Mayer, B.: Aviation induced diurnal North Atlantic cirrus cover cycle, Geophysical Research Letters, 39, https://doi.org/10.1029/2012GL052590, _eprint: https://agupubs.onlinelibrary.wiley.com/doi/pdf/10.1029/2012GL052590, 2012.

Hallam, S., Josey, S. A., McCarthy, G. D., and Hirschi, J. J.-M.: A regional (land–ocean) comparison of the seasonal to decadal variability of the Northern Hemisphere jet stream 1871–2011, Climate Dynamics, 59, 1897–1918, https://doi.org/10.1007/s00382-022-06185-5, 2022.

Hoerl, A. E. and Kennard, R. W.: Ridge Regression: Biased Estimation for Nonorthogonal Problems, 12, 1970.

Holmlund, K., Grandell, J., Schmetz, J., Stuhlmann, R., Bojkov, B., Munro, R., Lekouara, M., Coppens, D., Viticchie, B., August, T., Theodore, B., Watts, P., Dobber, M., Fowler, G., Bojinski, S., Schmid, A., Salonen, K., Tjemkes, S., Aminou, D., and Blythe, P.: Meteosat Third Generation (MTG): Continuation and Innovation of Observations from Geostationary Orbit, Bulletin of the American Meteorological Society, 102, E990–E1015, https://doi.org/10.1175/BAMS-D-19-0304.1, 2021.

Irvine, E. A., Hoskins, B. J., and Shine, K. P.: The dependence of contrail formation on the weather pattern and altitude in the North Atlantic, Geophysical Research Letters, 39, https://doi.org/10.1029/2012GL051909, 2012.

Klöwer, M., Allen, M. R., Lee, D. S., Proud, S. R., Gallagher, L., and Skowron, A.: Quantifying aviation's contribution to global warming, Environmental Research Letters, 16, 104 027, https://doi.org/10.1088/1748-9326/ac286e, 2021.

Kox, S., Bugliaro, L., and Ostler, A.: Retrieval of cirrus cloud optical thickness and top altitude from geostationary remote sensing, Atmospheric Measurement Techniques, 7, 3233–3246, https://doi.org/10.5194/amt-7-3233-2014, 2014.

Kärcher, B.: Formation and radiative forcing of contrail cirrus, Nature Communications, 9, 1824, https://doi.org/10.1038/s41467-018-04068-0, 2018.

Kärcher, B., Burkhardt, U., Bier, A., Bock, L., and Ford, I. J.: The microphysical pathway to contrail formation, Journal of Geophysical Research: Atmospheres, 120, 7893–7927, https://doi.org/10.1002/2015JD023491, _eprint: https://agupubs.onlinelibrary.wiley.com/doi/pdf/10.1002/2015JD023491, 2015.

Laken, B. A., Pallé, E., Kniveton, D. R., Williams, C. J. R., and Kilham, D. A.: Contrails developed under frontal influences of the North Atlantic, Journal of Geophysical Research: Atmospheres, 117, https://doi.org/10.1029/2011JD017019, 2012.

Lee, D. S., Fahey, D. W., Skowron, A., Allen, M. R., Burkhardt, U., Chen, Q., Doherty, S. J., Freeman, S., Forster, P. M., Fuglestvedt, J., Gettelman, A., De León, R. R., Lim, L. L., Lund, M. T., Millar, R. J., Owen, B., Penner, J. E., Pitari, G., Prather, M. J., Sausen, R., and Wilcox, L. J.: The contribution of global aviation to anthropogenic climate forcing for 2000 to 2018, Atmospheric Environment, 244, 117 834, https://doi.org/10.1016/j.atmosenv.2020.117834, 2021.

Mannstein, H., Meyer, R., and Wendling, P.: Operational detection of contrails from NOAA-AVHRR-data, International Journal of Remote Sensing, 20, 1641–1660, https://doi.org/10.1080/014311699212650, _eprint: https://doi.org/10.1080/014311699212650, 1999.

Mannstein, H., Brömser, A., and Bugliaro, L.: Ground-based observations for the validation of contrails and cirrus detection in satellite imagery, Atmospheric Measurement Techniques, 3, 655–669, https://doi.org/10.5194/amt-3-655-2010, 2010.

Mayer, J., Bugliaro, L., Mayer, B., Piontek, D., and Voigt, C.: Bayesian cloud-top phase determination for Meteosat Second Generation, Atmospheric Measurement Techniques, 17, 4015–4039, https://doi.org/10.5194/amt-17-4015-2024, 2024.

Meerkötter, R., Schumann, U., Doelling, D. R., Minnis, P., Nakajima, T., and Tsushima, Y.: Radiative forcing by contrails, Annales Geophysicae, 17, 1080–1094, https://doi.org/10.1007/s00585-999-1080-7, 1999.

Meijer, V. R., Kulik, L., Eastham, S. D., Allroggen, F., Speth, R. L., Karaman, S., and Barrett, S. R. H.: Contrail coverage over the United States before and during the COVID-19 pandemic, Environmental Research Letters, 17, 034 039, https://doi.org/10.1088/1748-9326/ac26f0, 2022.

Meijer, V. R., Eastham, S. D., Waitz, I. A., and Barrett, S. R. H.: Contrail altitude estimation using GOES-16 ABI data and deep learning, Atmospheric Measurement Techniques, 17, 6145–6162, https://doi.org/10.5194/amt-17-6145-2024, 2024.

Minnis, P., Young, D. F., Garber, D. P., Nguyen, L., Smith Jr., W. L., and Palikonda, R.: Transformation of contrails into cirrus during SUCCESS, Geophysical Research Letters, 25, 1157–1160, https://doi.org/10.1029/97GL03314, _eprint: https://onlinelibrary.wiley.com/doi/pdf/10.1029/97GL03314, 1998.

Minnis, P., Palikonda, R., Walter, B. J., Ayers, J. K., and Mannstein, H.: Contrail properties over the eastern North Pacific from AVHRR data, Meteorologische Zeitschrift, pp. 515–523, https://doi.org/10.1127/0941-2948/2005/0056, 2005.

Ng, J., Elkin, C., Sarna, A., Reade, W., and Demkin, M.: Google Research - Identify Contrails to Reduce Global Warming, https://kaggle.com/competitions/google-research-identify-contrails-reduce-global-warming, 2023a.

Ng, J. Y.-H., McCloskey, K., Cui, J., Meijer, V. R., Brand, E., Sarna, A., Goyal, N., Van Arsdale, C., and Geraedts, S.: OpenContrails: Benchmarking Contrail Detection on GOES-16 ABI, https://doi.org/10.48550/arXiv.2304.02122, arXiv:2304.02122 [cs], 2023b.

Ng, J. Y.-H., McCloskey, K., Cui, J., Meijer, V. R., Brand, E., Sarna, A., Goyal, N., Van Arsdale, C., and Geraedts, S.: Contrail Detection on GOES-16 ABI With the OpenContrails Dataset, IEEE Transactions on Geoscience and Remote Sensing, 62, 1–14, https://doi.org/10.1109/TGRS.2023.3345226, conference Name: IEEE Transactions on Geoscience and Remote Sensing, 2024.

OpenSky: Open Air Traffic Data for Research, https://opensky-network.org/, 2026.

Ortiz, I., García-Heras, J., Jafarimoghaddam, A., and Soler, M.: Robust Evaluation of OpenContrails Neural Networks with Temporal Corrections via Optical Flow, IEEE Transactions on Geoscience and Remote Sensing, pp. 1–1, https://doi.org/10.1109/TGRS.2025.3629628, 2025.

Palikonda, R., Minnis, P., Duda, D. P., and Mannstein, H.: Contrail coverage derived from 2001 AVHRR data over the continental United States of America and surrounding areas, Meteorologische Zeitschrift, pp. 525–536, https://doi.org/10.1127/0941-2948/2005/0051, 2005.

Santos Gabriel, V., Bugliaro, L., Montag, M., Ries, S., Wang, Z., Widmaier, K., Arico, M., Unterstrasser, S., Mayer, J., Menekay, D., Marsing, A., de la Torre Castro, E., Megill, L., Scheibe, M., and Voigt, C.: A manually labeled contrail dataset from MSG/SEVIRI, Earth System Science Data, 18, 2397–2412, https://doi.org/10.5194/essd-18-2397-2026, 2026.

Sanz-Morère, I., Eastham, S. D., Allroggen, F., Speth, R. L., and Barrett, S. R. H.: Impacts of multi-layer overlap on contrail radiative forcing, Atmospheric Chemistry and Physics, 21, 1649–1681, https://doi.org/10.5194/acp-21-1649-2021, 2021.

Schmetz, J., Pili, P., Tjemkes, S., Just, D., Kerkmann, J., Rota, S., and Ratier, A.: AN INTRODUCTION TO METEOSAT SECOND GENERATION (MSG), https://journals.ametsoc.org/view/journals/bams/83/7/1520-0477_2002_083_0977_aitmsg_2_3_co_2.xml, 2002.

Schumann, U.: A contrail cirrus prediction model, Geoscientific Model Development, 5, 543–580, https://doi.org/10.5194/gmd-5-543-2012, 2012.

Schumann, U. and Heymsfield, A. J.: On the Life Cycle of Individual Contrails and Contrail Cirrus, Meteorological Monographs, 58, 3.1–3.24, https://doi.org/10.1175/AMSMONOGRAPHS-D-16-0005.1, 2017.

Schumann, U., Mayer, B., Graf, K., and Mannstein, H.: A Parametric Radiative Forcing Model for Contrail Cirrus, https://doi.org/10.1175/JAMC-D-11-0242.1, 2012.

Sonabend-W, A., Geraedts, S., Goyal, N., Ng, J. Y.-H., Van Arsdale, C., and McCloskey, K.: Observing long-lived longwave contrail forcing, https://doi.org/10.5194/egusphere-2025-3739, 2025.

Spangenberg, D. A., Minnis, P., Bedka, S. T., Palikonda, R., Duda, D. P., and Rose, F. G.: Contrail radiative forcing over the Northern Hemisphere from 2006 Aqua MODIS data, Geophysical Research Letters, 40, 595–600, https://doi.org/10.1002/grl.50168, _eprint: https://agupubs.onlinelibrary.wiley.com/doi/pdf/10.1002/grl.50168, 2013.

Strandgren, J., Bugliaro, L., Sehnke, F., and Schröder, L.: Cirrus cloud retrieval with MSG/SEVIRI using artificial neural networks, Atmospheric Measurement Techniques, 10, 3547–3573, https://doi.org/10.5194/amt-10-3547-2017, 2017a.

Strandgren, J., Fricker, J., and Bugliaro, L.: Characterisation of the artificial neural network CiPS for cirrus cloud remote sensing with MSG/SEVIRI, Atmospheric Measurement Techniques, 10, 4317–4339, https://doi.org/10.5194/amt-10-4317-2017, 2017b.

Teoh, R., Schumann, U., Gryspeerdt, E., Shapiro, M., Molloy, J., Koudis, G., Voigt, C., and Stettler, M. E. J.: Aviation contrail climate effects in the North Atlantic from 2016 to 2021, Atmospheric Chemistry and Physics, 22, 10 919–10 935, https://doi.org/10.5194/acp-22-10919-2022, 2022.

Teoh, R., Engberg, Z., Schumann, U., Voigt, C., Shapiro, M., Rohs, S., and Stettler, M. E. J.: Global aviation contrail climate effects from 2019 to 2021, Atmospheric Chemistry and Physics, 24, 6071–6093, https://doi.org/10.5194/acp-24-6071-2024, 2024.

Vazquez-Navarro, M., Mannstein, H., and Mayer, B.: An automatic contrail tracking algorithm, Atmospheric Measurement Techniques, 3, 1089–1101, https://doi.org/10.5194/amt-3-1089-2010, 2010.

Vázquez-Navarro, M., Mannstein, H., and Kox, S.: Contrail life cycle and properties from 1 year of MSG/SEVIRI rapid-scan images, Atmospheric Chemistry and Physics, 15, 8739–8749, https://doi.org/10.5194/acp-15-8739-2015, 2015.

Wang, X., Wolf, K., Boucher, O., and Bellouin, N.: Radiative Effect of Two Contrail Cirrus Outbreaks Over Western Europe Estimated Using Geostationary Satellite Observations and Radiative Transfer Calculations, Geophysical Research Letters, 51, e2024GL108 452, https://doi.org/10.1029/2024GL108452, _eprint: https://onlinelibrary.wiley.com/doi/pdf/10.1029/2024GL108452, 2024.

Wang, Z., Bugliaro, L., Jurkat-Witschas, T., Heller, R., Burkhardt, U., Ziereis, H., Dekoutsidis, G., Wirth, M., Groß, S., Kirschler, S., Kaufmann, S., and Voigt, C.: Observations of microphysical properties and radiative effects of a contrail cirrus outbreak over the North Atlantic, Atmospheric Chemistry and Physics, 23, 1941–1961, https://doi.org/10.5194/acp-23-1941-2023, 2023.

Watts, P. D., Bennartz, R., and Fell, F.: Retrieval of two-layer cloud properties from multispectral observations using optimal estimation, Journal of Geophysical Research: Atmospheres, 116, https://doi.org/10.1029/2011JD015883, 2011.

Wehr, T., Kubota, T., Tzeremes, G., Wallace, K., Nakatsuka, H., Ohno, Y., Koopman, R., Rusli, S., Kikuchi, M., Eisinger, M., Tanaka, T., Taga, M., Deghaye, P., Tomita, E., and Bernaerts, D.: The EarthCARE mission – science and system overview, Atmospheric Measurement Techniques, 16, 3581–3608, https://doi.org/10.5194/amt-16-3581-2023, 2023.

Wolf, K., Bellouin, N., and Boucher, O.: Sensitivity of cirrus and contrail radiative effect on cloud microphysical and environmental parameters, Atmospheric Chemistry and Physics, 23, 14 003–14 037, https://doi.org/10.5194/acp-23-14003-2023, 2023.

Supplementary Files

This is a list of supplementary files associated with this preprint. Click to download.

- 2023paperAMT7.pdf